GEOPHYSICS, VOL. 82, NO. 4 (JULY-AUGUST 2017); P. G57–G69, 11 FIGS.
10.1190/GEO2016-0332.1

Fast iterative equivalent-layer technique for gravity data processing: A method grounded on excess mass constraint

Fillipe C. L. Siqueira[1], Vanderlei C. Oliveira Jr.[1], and Valéria C. F. Barbosa[1]

ABSTRACT

We have developed a new iterative scheme for processing gravity data using a fast equivalent-layer technique. This scheme estimates a 2D mass distribution on a fictitious layer located below the observation surface and with finite horizontal dimensions composed by a set of point masses, one directly beneath each gravity station. Our method starts from an initial mass distribution that is proportional to the observed gravity data. Iteratively, our approach updates the mass distribution by adding mass corrections that are proportional to the gravity residuals. At each iteration, the computation of the residual is accomplished by the forward modeling of the vertical component of the gravitational attraction produced by all point masses setting up the equivalent layer. Our method is grounded on the excess of mass and on the positive correlation between the observed gravity data and the masses on the equivalent layer. Mathematically, the algorithm is formulated as an iterative least-squares method that requires neither matrix multiplications nor the solution of linear systems, leading to the processing of large data sets. The time spent on the forward modeling accounts for much of the total computation time, but this modeling demands a small computational effort. We numerically prove the stability of our method by comparing our solution with the one obtained via the classic equivalent-layer technique with the zeroth-order Tikhonov regularization. After estimating the mass distribution, we obtain a desired processed data by multiplying the matrix of the Green's functions associated with the desired processing by the estimated mass distribution. We have applied the proposed method to interpolate, calculate the horizontal components, and continue gravity data upward (or downward). Testing on field data from the Vinton salt dome, Louisiana, USA, confirms the potential of our approach in processing large gravity data set over on undulating surface.

INTRODUCTION

Since the late 1960s, the equivalent-layer technique has been used for processing potential field data. Mathematically, the equivalent layer is a consequence of solving Laplace's equation (Kellogg, 1929) in the source-free region above the observation surface using the observed field as the Dirichlet boundary condition. Based on potential theory, a continuous record of a potential field data produced by any source can be exactly reproduced by a fictitious, continuous, and infinite 2D physical-property surface distribution that is called the equivalent layer. To our knowledge, Dampney (1969) is the pioneer on the approximation of the continuous equivalent layer by a discrete layer. In Dampney (1969), a discrete set of potential field observations produced by any source can be exactly reproduced by a fictitious layer located below the observation surface and with finite horizontal dimensions composed by a finite discrete set of equivalent sources.

The equivalent-layer technique has been used for (1) interpolating and gridding data (e.g., Cordell, 1992; Mendonça and Silva, 1994), (2) computing the upward (or downward) continuation of data (e.g., Emilia, 1973; Hansen and Miyazaki, 1984; Li and Oldenburg, 2010), (3) computing the reduction to the pole of magnetic data (e.g., Silva, 1986; Leão and Silva, 1989; Guspí and Novara, 2009; Oliveira et al., 2013), (4) merging multiple data sets (Boggs and Dransfield, 2004; Lane, 2004), and (5) jointly processing multiple components of airborne gravity gradient data (e.g., Barnes and Lumley, 2011).

The classic equivalent-layer technique consists of constructing a linear system of equations and solving a linear inverse problem to estimate a set of coefficients describing a discrete layer of equivalent sources. Usually, the equivalent-layer technique deals with large-

Manuscript received by the Editor 22 June 2016; revised manuscript received 11 February 2017; published online 05 May 2017.
[1]Observatório Nacional, Rio de Janeiro, Brazil. E-mail: fillipesiqueira@gmail.com; vandscoelho@gmail.com; valcris@on.br.

scale matrix computations for processing large data sets. This disadvantage propels the development of computational strategies to make the equivalent-layer technique computationally efficient. Leão and Silva (1989) are the pioneers in designing a equivalent-layer scheme that is able to efficiently handle large-scaled problems. They develop a fast moving-window scheme spanning the whole data set. In this scheme, the potential field processing is only computed at the center of a small moving-equivalent-source window. Hence, Leão and Silva (1989) solve several small linear systems, instead of solving a single large linear system involving the entire equivalent layer. Following the same strategy of solving successive small linear systems, Mendonça and Silva (1994) propose the equivalent data concept. It consists of obtaining automatically an equivalent data set that is a data subset smaller than the total number of observations. In this scheme, the interpolated surface that fits the chosen equivalent data set al.o fits the remaining data automatically.

Following the strategy of compressing the linear system of equations associated with the equivalent-layer technique, Li and Oldenburg (2010) use a wavelet compression and Davis and Li (2011) combine an adaptive mesh and wavelet compression. Barnes and Lumley (2011) reduce the computational load by grouping a set of equivalent sources that lie distant from the ith observation into an average equivalent source, leading to a sparse linear system. Oliveira et al. (2013) reduce the number of unknown parameters by assuming that the physical-property distribution within the equivalent layer can be approximated by a piecewise-polynomial function defined on a set of equivalent source windows. This procedure estimates the polynomial coefficients for each equivalent source window, and next, these coefficients are transformed into the physical-property distribution within an equivalent layer. Following the strategy of using the equivalent-layer technique without solving a system of linear equations, the physical-property distribution of each equivalent source is updated iteratively. Xia and Sprowl (1991) update the physical-property distribution by using the ratio between the squared depth to the equivalent source and the gravitational constant multiplied by the misfit between the measured and the calculated anomalies at the measurement stations. Xia et al. (1993) use an iterative scheme in the wavenumber domain. Cordell (1992) updates the physical-property distribution by an iterative procedure that removes the maximum residual until all residuals become bounded by an envelope with a prefixed semiamplitude related to the expected noise level. Guspí and Novara (2009) modify the iterative Cordell's (1992) method to reduce the total-field anomaly to the pole.

Faced with the demand for a fast and computationally efficient equivalent-layer method able to handle large data sets, we developed a new iterative equivalent-layer technique that does not solve linear systems. In our method, the equivalent layer is formed by a set of point masses, each one directly beneath each observation point. The iterative process starts from a mass distribution over the equivalent layer, whose ith mass is proportional to the ith gravity observation. Iteratively, the correction of the mass distribution consists in adding to the ith mass a quantity that is proportional to the ith gravity residual. In all mass distributions (initial and iterative corrections), the coefficient of proportionality is given by the ratio of the average area between data points to the constant $2\pi\gamma$, where γ is Newton's gravitational constant. We validate our method using synthetic and field examples.

METHODOLOGY

Consider a Cartesian coordinate system $x-y-z$ with z being positive downward, x directed toward the north, and y directed toward the east. Let $g(\epsilon, \eta, z_o)$ be the gravity data produced by a source distribution located entirely below the plane z_o. In this work, we consider that the gravity data are properly corrected from nongravitational effects, so that it represents the harmonic function defining the vertical component of the gravitational attraction produced by the sources. This means that, rigorously, the term gravity data used throughout this work is consistent with the gravity disturbance instead of the gravity anomaly. In this case, the Dirichlet integral, which is also called the upward continuation integral (Henderson, 1960, 1970), relates the gravity data $g(\epsilon, \eta, z_o)$ on the plane z_o to the gravity data $g_i \equiv g(x_i, y_i, z_i)$ at an arbitrary point (x_i, y_i, z_i),

$$g_i = \frac{1}{2\pi}\int_{-\infty}^{+\infty}\int_{-\infty}^{+\infty} g(\epsilon, \eta, z_o)\partial_z\theta(x_i-\epsilon, y_i-\eta, z_i-z_o)d\epsilon d\eta, \tag{1}$$

where $z_i < z_o$, $i = 1, \ldots, N$, $\partial_z\theta(x_i-\epsilon, y_i-\eta, z_i-z_o) \equiv (\partial\theta(x_i-\epsilon, y_i-\eta, z_i-z_o))/\partial z$ is the vertical derivative of the function:

$$\theta(x-\epsilon, y-\eta, z-z_o) = \frac{1}{r}, \tag{2}$$

where $r = [(x-\epsilon)^2 + (y-\eta)^2 + (z-z_o)^2]^{1/2}$.

By multiplying and dividing equation 1 by γ (Newton's gravitational constant) and discretizing the integrand in a set of points $(\epsilon_j, \eta_j, z_o)$, $j = 1, \ldots, N$, the surface integral can be numerically approximated by

$$g_i = \sum_{j=1}^{N} m_j a_{ij}, \quad i = 1, \ldots, N, \tag{3}$$

where m_j is the coefficients given by

$$m_j = \frac{\Delta s_j g_j'}{2\pi\gamma}, \quad j = 1, \ldots, N, \tag{4}$$

$g_j' \equiv g(\epsilon_j, \eta_j, z_o)$ is the gravity data at the jth coordinate point $(\epsilon_j, \eta_j, z_o)$, Δs_j is an element of area centered at $(\epsilon_j, \eta_j, z_o)$, and a_{ij} is a harmonic function given by

$$a_{ij} = \gamma\frac{(z_o - z_i)}{[(x_i-\epsilon_j)^2 + (y_i-\eta_j)^2 + (z_i-z_o)^2]^{\frac{3}{2}}}. \tag{5}$$

This harmonic function represents the Green's function of the vertical component of the gravitational attraction exerted at the ith observation point (x_i, y_i, z_i) by a point mass located at the point $(\epsilon_j, \eta_j, z_o)$.

Equation 3 represents the classic approach of the equivalent layer, in which the gravity data g_i at the ith observation point (x_i, y_i, z_i) are approximated by the sum of the vertical component of the gravitational attraction produced by a set of N fictitious equivalent sources (e.g., point masses) distributed on a horizontal plane at constant depth z_o, each one with mass m_j (equation 4). In matrix notation, equation 3 can be expressed as

$$\mathbf{g} = \mathbf{A}\mathbf{m}, \tag{6}$$

where $\mathbf{g}$ is an N-dimensional predicted data vector whose ith element is the gravity data g_i (equation 3), $\mathbf{A}$ is an $N \times N$ sensitivity matrix whose ijth element is defined by the harmonic function a_{ij} (equation 3), and $\mathbf{m}$ is the parameter vector whose jth element is the mass m_j (equation 4) of the jth equivalent source. Notice that the parameter vector $\mathbf{m}$ represents the physical-property distribution on the fictitious layer of equivalent sources.

Given an N-dimensional observed data vector $\mathbf{g^o}$ whose ith element is the observed gravity data g_i^o at the point (x_i, y_i, z_i), the estimate of the parameter vector $\mathbf{m}$ (equation 6) yielding an acceptable data fit usually involves the constrained optimization problem of minimizing the function,

$$\phi(\mathbf{m}) = \phi_g(\mathbf{m}) + \mu\phi_m(\mathbf{m}), \tag{7}$$

where $\phi_m(\mathbf{m})$ is a regularizing function, μ is the regularizing parameter, and $\phi_g(\mathbf{m})$ is the data-misfit function defined as

$$\phi_g(\mathbf{m}) = \|\mathbf{g^o} - \mathbf{g}\|_2^2, \tag{8}$$

which represents the squared Euclidean norm of the difference between the observed data $\mathbf{g^o}$ and the predicted data $\mathbf{g}$ (equation 6).

In equation 7, for example, the regularizing function can be the zeroth- or first-order Tikhonov regularizations (Tikhonov and Arsenin, 1977; Aster et al., 2005). If, just for illustration, the zeroth-order Tikhonov regularization is taken, the vector of parameter estimates $\mathbf{m}^*$ that minimizes the function $\phi(\mathbf{m})$ (equation 7) can be written as (Menke, 1989)

$$\mathbf{m}^* = (\mathbf{A}^\top\mathbf{A} + \mu\mathbf{I})^{-1}\mathbf{A}^\top\mathbf{g^o}, \tag{9}$$

where $\mathbf{I}$ is the identity matrix.

We stress that the linear system in the equivalent-layer problem (equation 9) usually involves a prohibitively computational cost. To overcome this difficulty, we propose an iterative equivalent-layer strategy grounded on the excess mass constraint.

Excess-mass constraint

From Gauss's theorem, the excess mass $\mathcal{M}$ of a body can be uniquely estimated as the surface integration of the gravity data $g(x, y, z_1)$ on a plane z_1 divided by a constant (Grant and West, 1965); i.e.,

$$\mathcal{M} = \frac{1}{2\pi\gamma}\int_{-\infty}^{+\infty}\int_{-\infty}^{+\infty} g(x, y, z_1)dxdy. \tag{10}$$

By substituting the upward continuation integral (equation 1) into the excess mass $\mathcal{M}$ (equation 10) and considering $z_i = z_1, i = 1, \ldots, N$, we get a new expression of the excess of mass given by

$$\mathcal{M} = \frac{1}{2\pi\gamma}\frac{z_o - z_1}{2\pi}\int_{-\infty}^{+\infty}\int_{-\infty}^{+\infty} g(\epsilon, \eta, z_o) \times\left[\int_{-\infty}^{+\infty}\int_{-\infty}^{+\infty}\frac{1}{[(x_i-\epsilon)^2+(y_i-\eta)^2+(z_1-z_o)^2]^{\frac{3}{2}}}dxdy\right]d\epsilon d\eta. \tag{11}$$

Because the bracketed surface integral is equal to $2\pi/z_o - z_1$ (Bhattacharyya, 1967), equation 11 is reduced to

$$\mathcal{M} = \frac{1}{2\pi\gamma}\int_{-\infty}^{+\infty}\int_{-\infty}^{+\infty} g(\epsilon, \eta, z_o)d\epsilon d\eta. \tag{12}$$

Equation 12 confirms that the excess mass $\mathcal{M}$ of a body is proportional to the surface integration of the gravity data $g(\epsilon, \eta, z_o)$ on a plane $z = z_o$ above the sources.

At first glance, the similarity between the well-known expression of the excess mass (equation 10) and the one given in equation 12 may seem strikingly obvious. This is not true because in equation 12, the horizontal plane $z = z_o$ is the one in which the equivalent sources are distributed and the gravity data $g(\epsilon, \eta, z_o)$ are over this plane. Equation 12 is not just mathematical deduction devoid of practical interest; rather, it will be used in this work.

Let us consider a sufficiently dense set of N gravity data $\mathbf{g} \equiv (g_1, \ldots, g_N)^\top$, where g_i is located at the ith coordinate point (x_i, y_i, z_i), with z_i, $i = 1, \ldots, N$, approximately constant. Then, the surface integral in equation 10 can be approximated by

$$\mathcal{M} \approx \frac{1}{2\pi\gamma}\mathbf{g}^\top\mathbf{\Delta s}, \tag{13}$$

where

$$\mathbf{\Delta s} \equiv (\Delta s_1, \ldots, \Delta s_N)^\top, \tag{14}$$

is an N-dimensional vector whose ith element Δs_i is an element of area located at the vertical coordinate z_i and centered at the horizontal coordinates (x_i, y_i), $i = 1, \ldots, N$. Similarly, the surface integral in equation 12 can be approximated by

$$\mathcal{M} \approx \frac{1}{2\pi\gamma}\mathbf{g}'^\top\mathbf{\Delta s}, \tag{15}$$

where $\mathbf{g}' \equiv (g_1, \ldots, g_N)^\top$ is an N-dimensional vector whose jth element g_j' (equation 4) represents the gravity data at the horizontal coordinates (ϵ_j, η_j) on the equivalent-layer plane located at depth z_o. By considering that the horizontal coordinates $\epsilon_j = x_i$ and $\eta_j = y_i$; then the vector $\mathbf{\Delta s}$ is given in equation 14.

By combining the jth mass m_j located on the equivalent layer at $(\epsilon_j, \eta_j, z_o)$ (equation 4) with equation 15, we obtain

$$\mathcal{M} \approx \sum_{j=1}^{N} m_j = \mathbf{1}^\top\mathbf{m}, \tag{16}$$

where $\mathbf{1}$ is an N-dimensional vector with all elements equal to one. From equations 13 and 16, we have

$$\frac{1}{2\pi\gamma}\mathbf{g}^\top\mathbf{\Delta s} \approx \mathbf{1}^\top\mathbf{m}. \tag{17}$$

Equation 17 shows that the sum of the gravity data $\mathbf{g}$ at the coordinates (x_i, y_i, z_i), $i = 1, \ldots, N$, is approximately proportional to the sum of the set of N masses forming the equivalent layer.

Let us assume a hypothetical equivalent layer that exactly fits a sufficiently dense set of N observed gravity data

$\mathbf{g^o} \equiv (g_1^o, \ldots, g_N^o)^\top$, where g_i^o is the observed gravity data at the ith coordinate point (x_i, y_i, z_i). Then, according to equation 17, we can establish the following approximation:

$$\frac{1}{2\pi\gamma}\mathbf{g^{o\top}}\mathbf{\Delta s} \approx \mathbf{1}^\top\mathbf{m^o}, \tag{18}$$

where $\mathbf{m^o}$ is an N-dimensional vector containing the mass distribution over a hypothetical equivalent layer.

By taking the difference between equations 17 and 18, we obtain

$$\frac{1}{2\pi\gamma}\mathbf{r}^\top\mathbf{\Delta s} \approx \mathbf{1}^\top\mathbf{\Delta m}, \tag{19}$$

where $\mathbf{\Delta m} = \mathbf{m^o} - \mathbf{m}$ is an N-dimensional vector containing mass differences within the equivalent layer and $\mathbf{r}$ is an N-dimensional residual vector of the gravity data; i.e.,

$$\mathbf{r} = \mathbf{g^o} - \mathbf{g}, \tag{20}$$

where $\mathbf{g}$ is given in equation 6. Notice that equation 19 sets an approximated relationship between the sum of residuals $\mathbf{r}$ and the sum of mass differences $\mathbf{\Delta m}$ within the equivalent layer. If we impose a positive correlation between the residual gravity data $\mathbf{r}$ and the masses $\mathbf{\Delta m}$ within the equivalent layer (equation 19), we obtain a new relationship given by

$$\tilde{\mathbf{A}}^{-1}\mathbf{r} = \mathbf{\Delta m}, \tag{21}$$

where $\tilde{\mathbf{A}}^{-1}$ is an $N \times N$ diagonal matrix defined by

$$\tilde{\mathbf{A}}^{-1} = \frac{1}{2\pi\gamma}\mathbf{\Delta}\mathcal{S}, \tag{22}$$

and $\mathbf{\Delta}\mathcal{S}$ is an $N \times N$ diagonal matrix whose main diagonal is defined the vector $\mathbf{\Delta s}$ (equation 14).

Equation 21 establishes an approximated linear relationship between each element of the residual vector $\mathbf{r}$ and each element of mass difference $\mathbf{\Delta m}$. We refer to equation 21 as excess mass constraint.

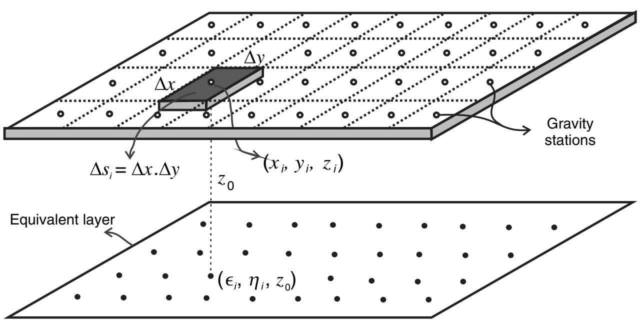

Figure 1. Schematic representation of an equivalent layer composed by a set of N point masses (black dots), one directly beneath each gravity station (open circles). The ith point mass is located at $(\epsilon_i, \eta_i, z_o)$ and the ith observed gravity data (x_i, y_i, z_i). The ith area Δs_i is ith element of the vector $\mathbf{\Delta s}$ (equation 14). For simplicity, a regular grid is displayed; however, an irregular grid can be used, as will be explained below.

Fast iterative equivalent layer algorithm

We propose an iterative scheme for estimating a mass distribution within an equivalent layer by minimizing the data-misfit function $\phi_g(\mathbf{m})$ (equation 8) with the excess mass constraint (equation 21). We consider a set of N point masses distributed in a layer located at depth z_o (Figure 1). We also consider that the horizontal position of the ith point mass (ϵ_i, η_i) coincides with the horizontal position of the ith observed gravity data (x_i, y_i). To use the excess mass constraint (equation 21) in our iterative method, we consider that, at the kth iteration, the mass-distribution estimate $\hat{\mathbf{m}}^k$ over the equivalent layer produces a predicted gravity data $\mathbf{g}^k$ (equation 6). From now on, the caret (^) denotes an estimate.

From the excess mass constraint (equation 21), we impose iteratively that

$$\mathbf{r}^k - \tilde{\mathbf{A}}\mathbf{\Delta}\hat{\mathbf{m}}^k \approx \mathbf{0}, \tag{23}$$

where $\mathbf{0}$ is the null vector, $\tilde{\mathbf{A}}$ is an $N \times N$ matrix defined as the inverse of the matrix $\tilde{\mathbf{A}}^{-1}$ (equation 22), $\mathbf{\Delta}\hat{\mathbf{m}}^k$ is the parameter correction estimate at the kth iteration, and $\mathbf{r}^k$ is the N-dimensional residual vector of the gravity data at the kth iteration; i.e.,

$$\mathbf{r}^k = \mathbf{g^o} - \mathbf{A}\hat{\mathbf{m}}^k. \tag{24}$$

Equation 23 imposes that, at the kth iteration, the mass correction estimate $\mathbf{\Delta}\hat{\mathbf{m}}^k$ must minimize the difference between the residuals $\mathbf{r}^k$ and the vector $\tilde{\mathbf{A}}\mathbf{\Delta}\hat{\mathbf{m}}^k$. Hence, our goal is to find a $\mathbf{\Delta}\hat{\mathbf{m}}^k$ such that the difference between the vectors $\mathbf{r}^k$ and $\tilde{\mathbf{A}}\mathbf{\Delta}\hat{\mathbf{m}}^k$ must be close to zero.

Mathematically, this mass correction estimate $\mathbf{\Delta}\hat{\mathbf{m}}^k$ can be found by minimizing, at the kth iteration, the function

$$\phi(\mathbf{\Delta m}^k) = \|\mathbf{g^o} - \mathbf{A}\hat{\mathbf{m}}^k - \tilde{\mathbf{A}}\mathbf{\Delta m}^k\|_2^2, \tag{25}$$

with respect to $\mathbf{\Delta m}^k$. Differentiating equation 25 with respect to $\mathbf{\Delta m}^k$ and setting the result equal to null vector, we obtain, at the kth iteration, the parameter correction estimate,

$$\mathbf{\Delta}\hat{\mathbf{m}}^k = \tilde{\mathbf{A}}^{-1}\mathbf{r}^k, \tag{26}$$

where the ith estimate is $\Delta\hat{m}_i^k = (\Delta s_i r_i^k)/2\pi\gamma$. This estimate represents the excess mass constraint (equation 21). After estimating the parameter correction vector at the kth iteration (equation 26), we update the mass distribution over the equivalent layer such that

$$\hat{\mathbf{m}}^{k+1} = \hat{\mathbf{m}}^k + \mathbf{\Delta}\hat{\mathbf{m}}^k. \tag{27}$$

The iterative process of our method starts with an initial approximation to the mass distributions over the equivalent layer given by

$$\mathbf{m}^0 = \tilde{\mathbf{A}}^{-1}\mathbf{g^o}, \tag{28}$$

where the ith initial approximation is $m_i^0 = (\Delta s_i g_i^o)/2\pi\gamma$. The iterative process stops when the data-misfit function (equation 8) and the estimated mass distribution over the equivalent data (equation 27) are invariant along successive iterations.

Iteratively, the fitted gravity data produced by the current approximation are removed from the observations $\mathbf{g}^o$, yielding a residual anomaly (equation 20) that is now used to compute a new parameter correction (equation 26). This iterative scheme works because, in practice, we have a positive correlation between the data and the parameter to be estimated in the equivalent layer. Thus, the larger the residual anomaly, the larger the parameter correction; hence, the better will be the fitted gravity data in the next iteration.

Finally, a desired linear transformation of the gravity data, such as horizontal components, interpolation, and upward (or downward) continuation, can be performed by

$$\mathbf{d}' = \mathbf{T}\hat{\mathbf{m}}, \tag{29}$$

where $\mathbf{d}'$ is an L-dimensional vector of the desired transformation, $\hat{\mathbf{m}}$ is the final estimated mass distribution on the equivalent layer, and $\mathbf{T}$ is an $L \times N$ matrix whose elements are the Green's function of the desired transformed gravity data.

To compute the x- and y-components of the gravity data, the ijth element of the matrix $\mathbf{T}$ is, respectively, equal to

$$T_{ij} = \frac{\gamma(x_j - x_i)}{[(x_i - x_j)^2 + (y_i - y_j)^2 + (z_i - z_o)^2]^{3/2}}, \tag{30}$$

and

$$T_{ij} = \frac{\gamma(y_j - y_i)}{[(x_i - x_j)^2 + (y_i - y_j)^2 + (z_i - z_o)^2]^{3/2}}, \tag{31}$$

where x_i, y_i, and z_i are the ith coordinate point of the ith observed gravity data and x_j, y_j, and z_o are the jth coordinate point of the jth equivalent mass on the equivalent layer.

To compute the interpolated vertical component of the gravitational attraction at the kth coordinate point x_k, y_k, and z_k, the kjth element of the matrix $\mathbf{T}$ is

$$T_{kj} = \frac{\gamma(z_o - z_k)}{[(x_k - x_j)^2 + (y_k - y_j)^2 + (z_k - z_o)^2]^{3/2}}. \tag{32}$$

The upward (or downward) continuation of the vertical component of the gravitational attraction is a special case of the interpolation, and hence the element of the matrix $\mathbf{T}$ is also given in equation 32. If z_k is lower (or greater) than the vertical coordinate of the measured data, then an upward (or downward) continuation is done.

Computation performance

In the classic equivalent-layer technique, the number of flops (an acronym for floating-point operations designed to carry out operations such as addition, subtraction, multiplication, and division) required to construct f_c and solve f_s the linear system of N equations in N unknowns (equation 9) are, respectively,

$$f_c = N^3 + N + 2N^2, \tag{33}$$

and

$$f_s = \frac{1}{3}N^3 + 2N^2. \tag{34}$$

In this analysis, we consider the solution of the linear system through the Cholesky factorization.

In our iterative equivalent-layer scheme, it is noticeable that the solution of linear systems is not required (equations 26–28). The number of flops in our scheme depends on the required number N^{it} of iterations and the mathematical operations in equations 26 and 27, and it is given by

$$f = N^{it}(3N + 2N^2), \tag{35}$$

where N is the number of gravity observations, and thus, the number of equivalent sources.

Figure 2 shows a graph of the number of observations N versus the computational demands using flops in the equivalent-layer

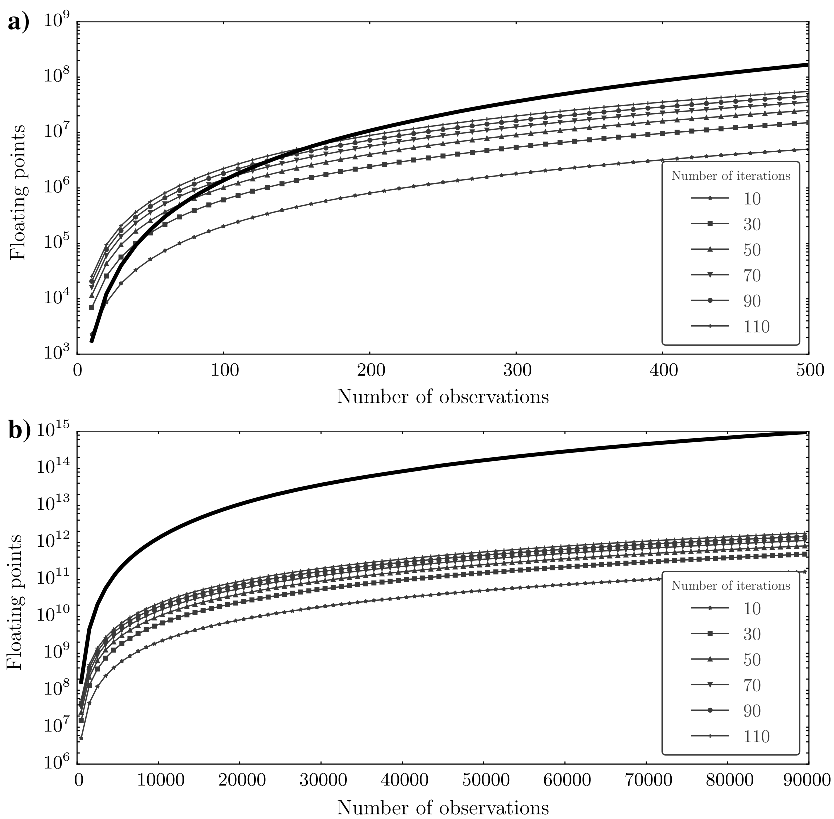

Figure 2. Graph of the number of observations N versus the floating-point operations required in the classic and in the fast iterative equivalent-layer techniques. The solid black thick lines show the floating-point operations (flops) required in the classic equivalent-layer technique that consists of the sum of equations 33 and 34. The adorned gray curves show the flops required in the fast iterative equivalent-layer technique (equation 35) using different numbers of iterations (10–110) and with the number of observations varying from (a) 10 to 500 and (b) 500 to 90,000.

technique. The flops required in the classic equivalent-layer technique are shown in the solid black line by summing equations 33 and 34. The adorned gray curves show the flops required in the fast iterative equivalent-layer technique using different numbers of iterations (equation 35).

By comparing the total number of flops required to estimate an equivalent layer via our method (the adorned gray curves in Figure 2) with the classic approach (the solid black line in Figure 2), we note that if the number of observations N is less than 500, the classic equivalent layer is better than our approach (Figure 2a). However, if the number of observations N is greater than 500 (Figure 2b), our approach has a much better computational efficiency, even using a large number of iterations (e.g., greater than 90).

SOLUTION STABILITY AND PRACTICAL PROCEDURES

Solution stability

We analyze numerically the solution stability obtained by the fast iterative equivalent-layer technique. By using a noise-free gravity data $\mathbf{g}$, we estimate a mass distribution $\mathbf{m}$ over the equivalent layer.

Next, we contaminate the noise-free data $\mathbf{g}$ with Q different sequences of pseudorandom numbers, generating different noise-corrupted gravity data $\mathbf{g}^{\mathbf{o}}_{\ell}$, $\ell = 1, \ldots, Q$. From each $\mathbf{g}^{\mathbf{o}}_{\ell}$, we estimate a mass distribution $\hat{\mathbf{m}}_{\ell}$ over the equivalent layer.

Then, for each noise-corrupted data $\mathbf{g}^{\mathbf{o}}_{\ell}$ and estimated mass distribution $\hat{\mathbf{m}}_{\ell}$, we computed the following quantities:

$$\delta m_{\ell} = \frac{\|\hat{\mathbf{m}}_{\ell} - \mathbf{m}\|_2}{\|\mathbf{m}\|_2}, \quad \ell = 1, \ldots, Q, \tag{36}$$

and

$$\delta g_{\ell} = \frac{\|\mathbf{g}^{\mathbf{o}}_{\ell} - \mathbf{g}\|_2}{\|\mathbf{g}\|_2}, \quad \ell = 1, \ldots, Q. \tag{37}$$

These quantities (equations 36 and 37) were calculated by using three different approaches: (1) the fast iterative equivalent-layer technique, (2) the classic equivalent-layer technique with zeroth-order Tikhonov regularization (equation 9), and (3) the least-squares method (equation 9 with $\mu = 0$).

According to the following inequality (Strang, 1988; Aster et al., 2005):

$$\delta m_{\ell} \leq \kappa \delta g_{\ell}, \quad \ell = 1, \ldots, Q, \tag{38}$$

the quantity δm_{ℓ} (equation 36) is proportional to δg_{ℓ} (equation 37), where κ is the proportionality constant. For the classic equivalent-layer technique with zeroth-order Tikhonov regularization (equation 9) and the least-squares method (equation 9 with $\mu = 0$), the constant κ represents the condition number of the matrices $(\mathbf{A}^{\mathrm{T}}\mathbf{A} + \mu\mathbf{I})$ and $(\mathbf{A}^{\mathrm{T}}\mathbf{A})$, respectively. A large κ indicates an unstable inverse problem, whereas a small κ indicates a stable inverse problem. Therefore, the slope of the line produced by plotting δm_{ℓ} (equation 36) as a function of δg_{ℓ} (equation 37) indicates the stability of the classic equivalent-layer technique with zeroth-order Tikhonov regularization (equation 9) and the least-squares method (equation 9 with $\mu = 0$).

In this work, we use the set of Q estimated mass distributions $\hat{\mathbf{m}}_{\ell}$ obtained by applying (1) the fast iterative equivalent-layer technique, (2) the classic equivalent-layer technique with zeroth-order Tikhonov regularization (equation 9), and (3) the least-squares method (equation 9 with $\mu = 0$) for generating three graphs of δm_{ℓ} (equation 36) versus δg_{ℓ} (equation 37). For each graph, we applied a linear regression and used the estimated slope of the fitted straight line to quantify the solution stability. Although our method does not solve a linear system, we used this approach to quantify the solution stability.

Practical procedures: Choice of z_o and $\Delta\mathbf{s}$

The practical procedures to use the fast iterative equivalent-layer technique require the choice of (1) the depth of the equivalent layer (z_o) and (2) the small areas to form the vector $\Delta\mathbf{s}$ (equations 14 and 22). Figure 1 shows z_o and the ith small area Δs_i related to the ith gravity observation that composed the vector $\Delta\mathbf{s}$.

The applications of our method show that, in practice, the equivalent layer can be placed at a constant depth z_o varying from 300 to 700 m below the average height of the gravity observations. An effective way to check if the choice of z_o was correctly done consists in verifying if the final estimated mass distribution yields an acceptable data fit. If the fitting is unsatisfactory, the depth of the equivalent layer must be changed.

Our method requires the definition of an average area between data points. The ith gravity data are associated with the ith area (Δs_i in Figure 1) that composes the vector $\Delta\mathbf{s}$ (equations 14 and 22). In practice, an average area between data points can be computed by dividing the whole survey area (in m^2) by the total number of observations. In this case, to all elements of the vector $\Delta\mathbf{s}$ will be assigned the computed average area. We can also compute a set of average areas, each one associated with a particular smaller region than the whole survey area. For example, let us assume a gravity survey with two flight patterns (I and II) each one with different number of data points per flight line and covering different regions (I and II) with distinct areas (in m^2). In this case, two average areas between data points can be computed, each one associated with one flight pattern (I and II). If the ith gravity observation lies inside the region I, the ith element of the vector $\Delta\mathbf{s}$ (equation 14) is computed by dividing the area of the flight pattern I (region I) by the number of data points in this region. Otherwise, if the ith gravity observation lies inside the region II, the ith element of the vector $\Delta\mathbf{s}$ is computed by dividing the area of the flight pattern II (region II) by the number of data points in this region.

TESTS WITH SYNTHETIC DATA

We investigate the performance of the proposed fast equivalent-layer technique in interpolating, calculating horizontal components, upward- and downward-continuing the synthetic gravity data produced by 18 3D prisms with density contrasts varying from −0.5 to 0.5 $\mathrm{g/cm^3}$. The simulated gravity data shown in Figure 3a are contaminated with Gaussian noise having a mean of zero and standard deviation of 0.067 mGal. The data are calculated over a simulated observation surface (Figure 3b). We used an irregular grid totaling 21,095 observation locations whose positions are shown in Figure 3c. We set the equivalent layer at constant depth 400 m. Because the simulated survey pattern has survey lines with different line spacing (dots in Figure 3c), we used three small areas to form the vector $\mathbf{\Delta s}$ that is used in equations 14 and 22. In this way, we divided the survey area into three distinct regions I–III shown in Figure 3c. If the ith gravity observation lies inside regions I and III, the ith element of the vector $\mathbf{\Delta s}$ (equation 14) is set to 13,416.0 m^2. On the other hand, if the ith gravity observation lies inside the region II, the ith element of the vector $\mathbf{\Delta s}$ is set to 5797.95 m^2. The estimated mass distribution (not shown) after 30 iterations of the fast equivalent-layer technique yields the fitted gravity anomaly shown in Figure 4a. Figure 4b shows the gravity residuals, defined as the difference between the observed and the predicted gravity data. The residuals appear normally distributed, with a mean of 0.0 mGal and a standard deviation of 0.07 mGal as shown in the histogram of residuals (inset in Figure 4b). For most of the area, the gravity residuals are approximately 0 mGal; then, the data fitting is acceptable, the estimated mass distribution can be accepted, and the desired data processing can be done, as shown below.

Horizontal components and interpolation

By using equation 29, we compute the x- and y-components of the gravity data with the estimated mass distribution $\hat{\mathbf{m}}$ within the equivalent layer (not shown) through equations 30 and 31, respectively.

The true and predicted north–south components of gravity data are shown in Figure 5a and 5b, respectively. The residuals (Figure 5c), defined as the difference between the true and predicted north–south components of gravity data, appear normally distributed, with a mean of 0.0 mGal and a standard deviation of 0.04 mGal. Figure 6a and 6b shows the true and predicted east–west components of gravity data. Figure 6c shows the corresponding residuals (the true minus predicted east–west components of gravity data). The histogram of residuals resembles a normal distribution with a mean of 0.0 mGal and a standard deviation of 0.03 mGal. Both histograms of the residuals of the horizontal components of the gravity data (insets of Figures 5c and 6c) corroborate the acceptance of the predicted north–south (Figure 5b) and east–west (Figure 6b) components of the gravity data by our method.

By using equation 32, we compute the interpolated vertical component of the gravitational attraction (Figure 3a) at a regular grid (not shown) consisting of 170 lines with 7000 points. These lines set up an interpolated pattern with 100 lines oriented north–south at 168 m spacing and 70 lines oriented east–west at 163.3 m spacing. The interpolated data were computed at the uneven surface shown in Figure 7a. Figure 7b and 7c shows the theoretical and interpolated vertical component of the gravitational attraction. The residuals (Figure 7d) and the histogram of residuals certify the good performance of our method in interpolating the vertical component of the gravitational attraction.

Upward and downward continuations

We perform upward and downward continuations of the synthetic gravity data (Figure 3a) on the same horizontal coordinates (Figure 3c) of the original data. The upward- and the downward-continued gravity data (Figure 8) were computed at variable z-coordinates (equation 32). Specifically, the z-coordinates in the upward continuation (Figure 8a) are calculated by subtracting from each z-coordinate of each observation point (Figure 3b) at a constant value of 500 m. Conversely, the z-coordinates in the downward continuation (Figure 8b) are calculated by adding from each z-coordinate of each observation point (Figure 3b) at a constant value of 100 m. Figure 8c and 8d shows the residuals and

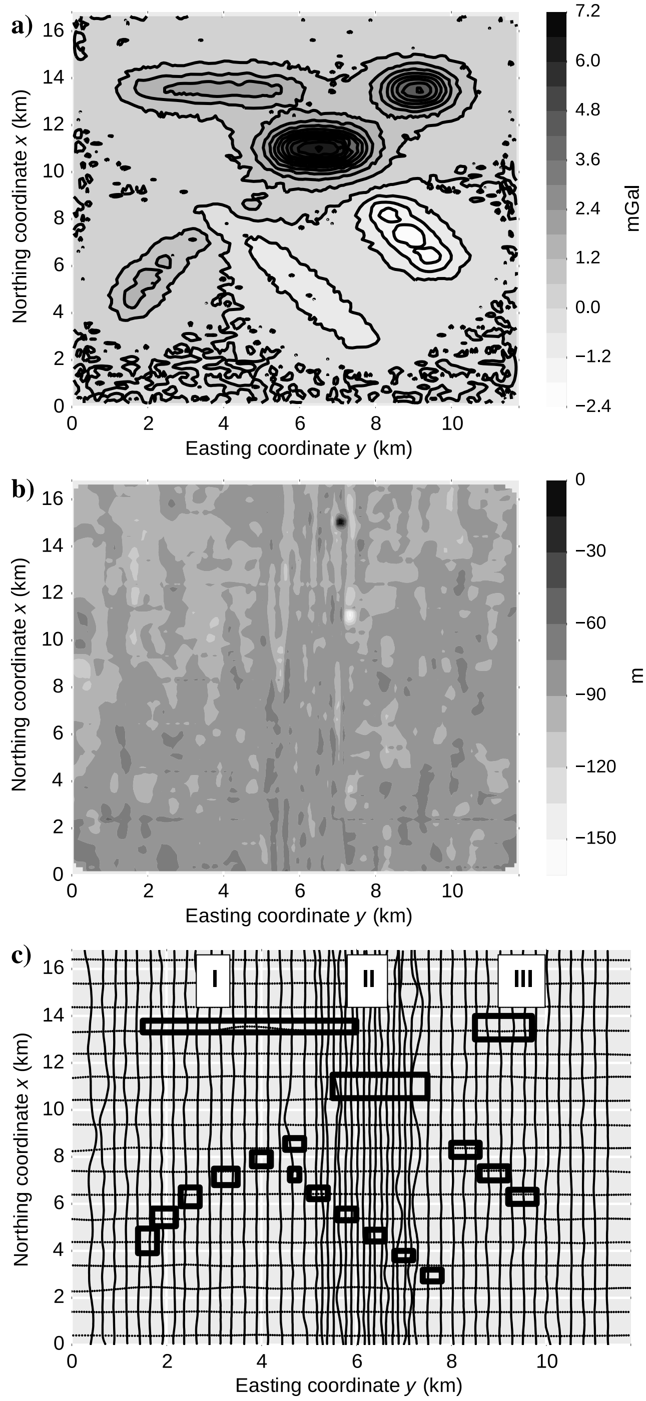

Figure 3. (a) Noise-corrupted gravity data (in grayscale map and contour curves) computed on (b) the simulated observation surface (in grayscale map). (c) The simulated flight line pattern with 21,095 observation locations (dots). The horizontal projections of the 18 sources are shown in panel (c) in black lines.

the histograms of the residuals (insets) in which residuals are defined as the difference between the true (not shown) and the upward- and the downward-continued gravity data. Because the residuals are approximately 0 mGal and the standard deviations are small, either the upward- or the downward-continued gravity data are accepted.

ANALYSIS OF SOLUTION STABILITY

We conducted a numerical analysis to investigate the solution stability of the fast iterative equivalent-layer technique. We first simulated noise-free gravity data produced by the same 18 sources described in the previous section. The data are calculated at -100 m height, on a regular grid of 55×55 observation points, with a grid spacing of 200 and 290.9 m along the x- and y-directions, respectively. We set an equivalent layer located at 200 m deep being composed by 55×55 point masses, one directly beneath each gravity observation.

First, we estimate three mass distributions $\mathbf{m}$ over the equivalent layer from the noise-free gravity data $\mathbf{g}$ by using (1) the fast iterative equivalent-layer technique, (2) the classic equivalent-layer technique with zeroth-order Tikhonov regularization (equation 9), and (3) the least-squares method (equation 9 with $\mu = 0$).

Next, we generate $Q = 40$ sequences of pseudorandom noise, and thus generate 40 sets of noise-corrupted gravity data ($\mathbf{g}^{\mathbf{o}}_{\ell}, \ell = 1, \ldots, 40$). Each sequence of pseudorandom noise has a

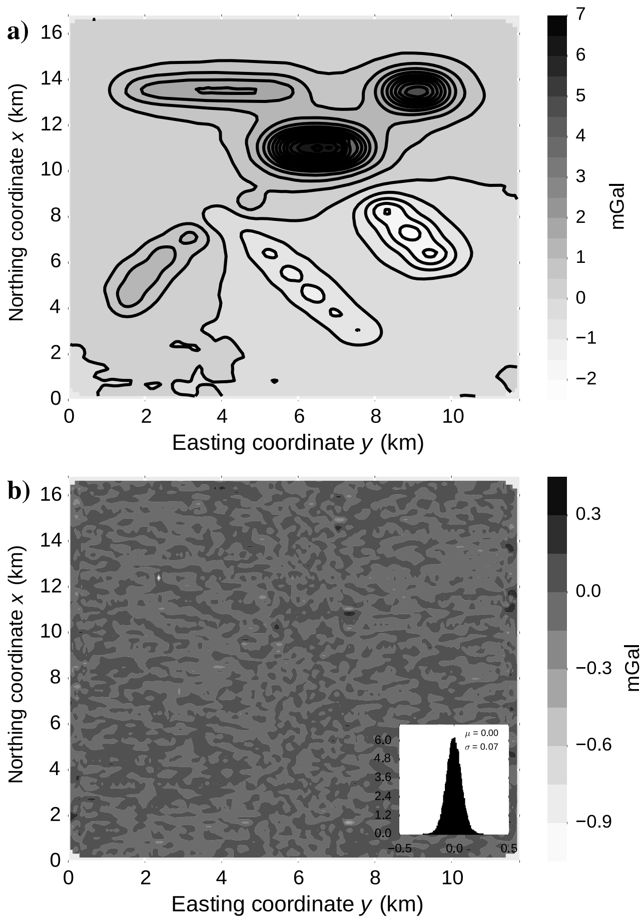

Figure 4. (a) Fitted gravity anomaly produced by the fast equivalent-layer technique. (b) Gravity residuals, defined as the difference between the synthetic noise-corrupted gravity data in Figure 3a and the predicted data in (a). The inset in (b) shows the histogram of gravity residuals shown in panel (b), with its mean μ and standard deviation σ in mGal.

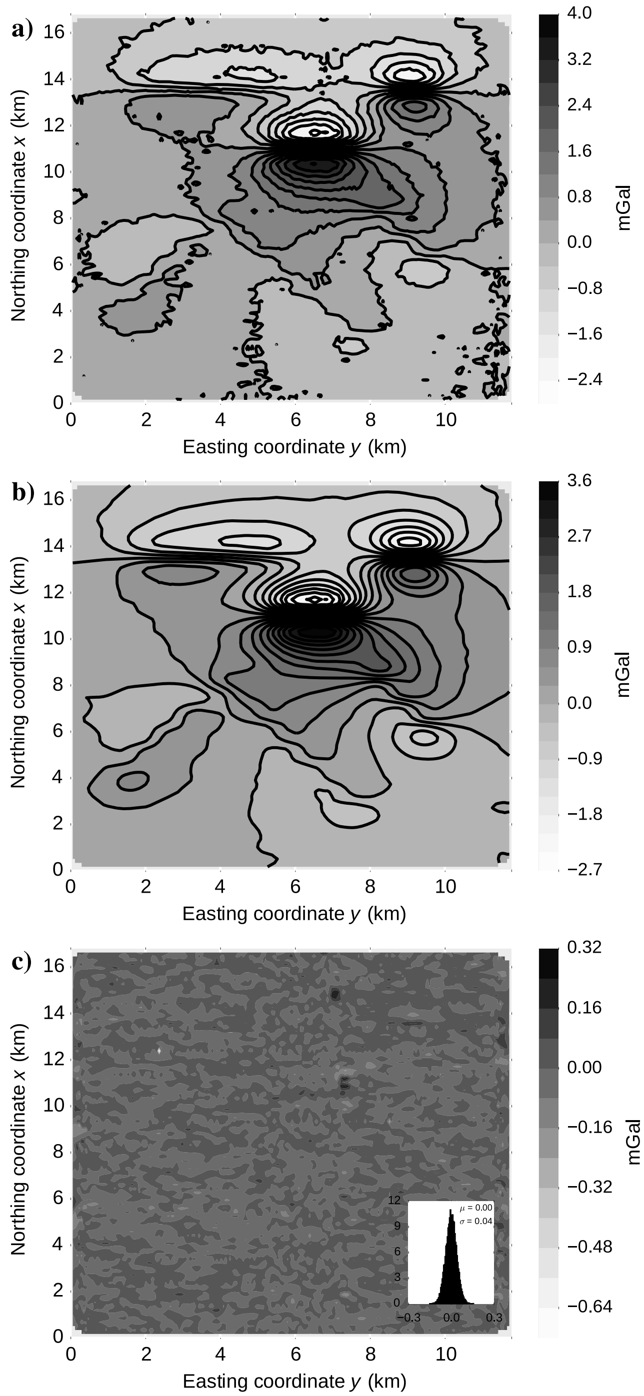

Figure 5. (a) True and (b) computed north–south components of gravity data. (c) Residuals, defined as the difference between the true in panel (a) and computed in panel (b) north–south components of the gravity data. The inset in panel (c) shows the histogram of residuals with its mean μ and standard deviation σ in mGal.

Gaussian distribution with zero mean and standard deviation varying from 1% to 10% of the maximum value of the noise-free gravity data. From the ℓth noise-corrupted gravity data $\mathbf{g}^{\mathbf{o}}_{\ell}$, we estimate three mass distributions $\hat{\mathbf{m}}_{\ell}$ over the equivalent layer by using

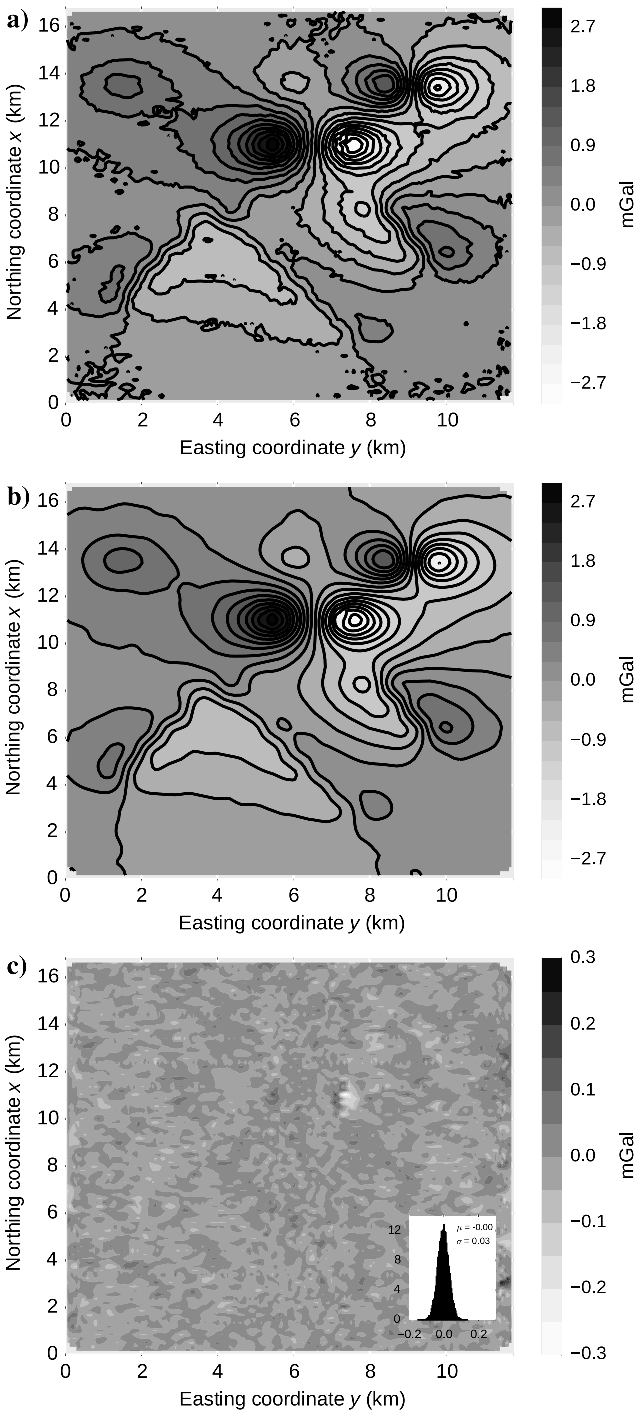

Figure 6. (a) True and (b) computed east–west components of gravity data. (c) Residuals, defined as the difference between the true in panel (a) and computed in panel (b) east–west components of the gravity data. The inset in (c) shows the histogram of residuals with its mean μ and standard deviation σ in mGal.

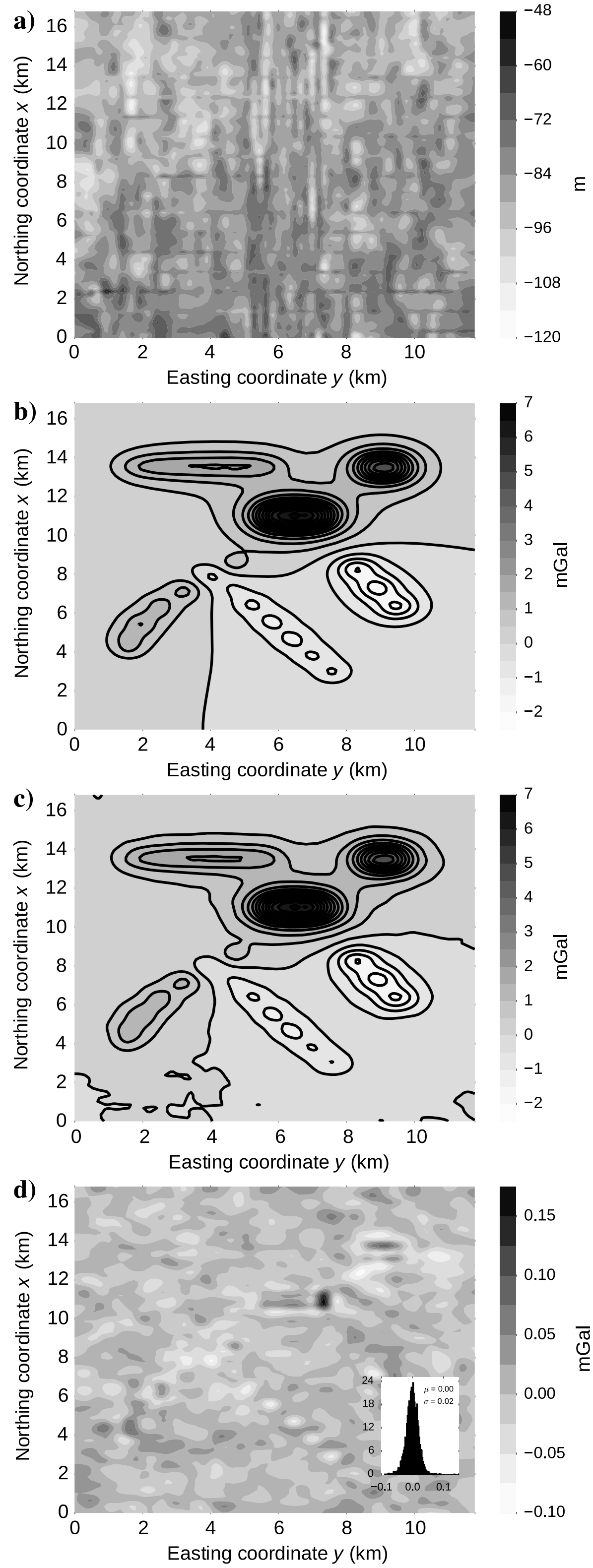

Figure 7. (a) Simulated uneven surface topography (in grayscale map) in which the gravity data will be interpolated. (b) True and (c) computed interpolated gravity data. (d) Residuals, defined as the difference between the true (not shown) and computed (shown in panel [c]) interpolated gravity data. The inset in panel (d) shows the histogram of residuals with its mean μ and standard deviation σ in mGal.

(1) the fast iterative equivalent-layer technique, (2) the classic equivalent-layer technique with the zeroth-order Tikhonov regularization (equation 9), and (3) the least-squares method (equation 9 with $\mu = 0$).

Then, we compute three sets of 40 δm_ℓ and δg_ℓ, $\ell = 1, \ldots, 40$ by using equations 36 and 37, respectively. In Figure 9a, the red, green, and yellow dots represent the 40 results obtained with the fast iterative equivalent-layer technique, the classic equivalent-layer technique with the zeroth-order Tikhonov regularization and least-squares method, respectively. By applying the linear regression, we obtain three fitted straight lines (red, green, and yellow lines in Figure 9a) whose estimated slopes represent the stability of the solution.

Notice in Figure 9a that the estimated slope obtained with the least-squares solutions (yellow line) is much greater than produced either by the fast iterative equivalent-layer technique (red line) and the classic equivalent layer with zeroth-order Tikhonov regularization (green line). The most striking feature in Figure 9a is that the estimated slopes produced by the fast iterative equivalent-layer technique (red line) and the zeroth-order Tikhonov regularization (green line) are close to each other. This result suggests that our method produces a stable solution.

By increasing the data set to an 85×85 regular grid of observations and applying this analysis, we obtained new estimated slopes (Figure 9b). As expected, the estimated slope obtained with the least-squares solutions (yellow line, in Figure 9b) is much greater than the one obtained in Figure 9a. However, we stress that the estimated slopes produced by the fast iterative equivalent-layer technique (red line in Figure 9b) and the classic equivalent-layer technique with the zeroth-order Tikhonov regularization (green line in Figure 9b) are close to each other and close to those ones estimated in Figure 9a. Similarly to the previous stability test, this new result confirms that our method produces stable solution even if the number of observations is increased.

TESTS WITH FIELD DATA

We test the proposed method on a real gravity data set over the Vinton salt dome, which lies within the onshore Gulf of Mexico located in southwestern Louisiana, USA. The dome is characterized by a massive cap rock extending above the salt rock (Coker et al., 2007). According to Ennen and Hall (2011) and Oliveira and Barbosa (2013), this cap rock is embedded in sediments characterized by intercalated layers of sandstone and shale.

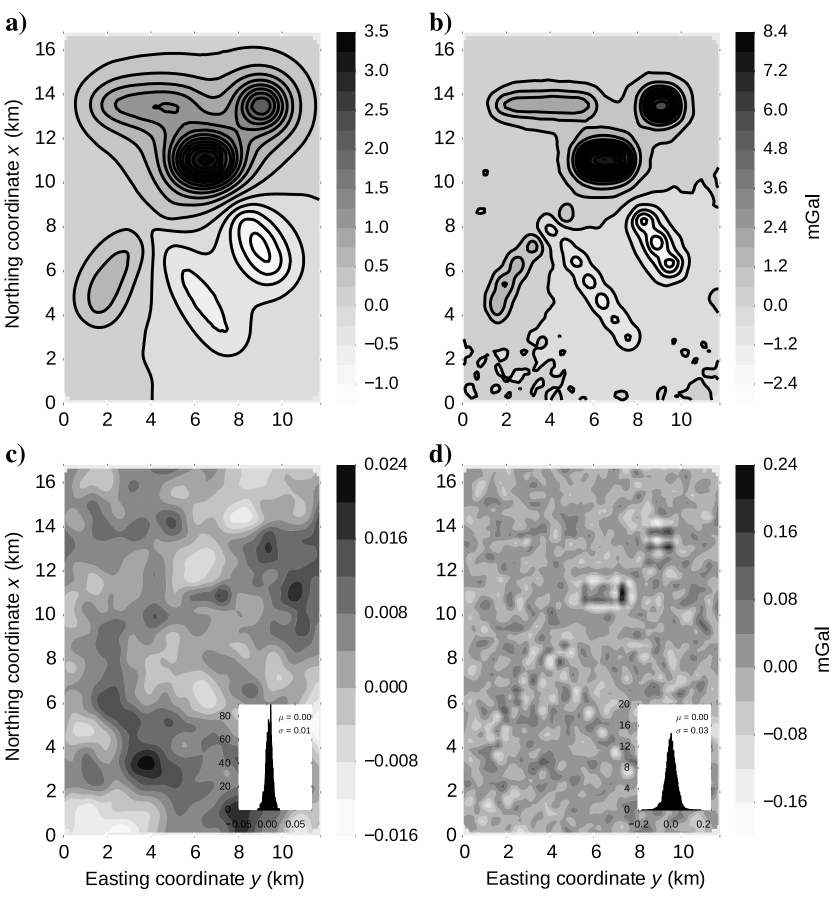

Figure 8. (a) Upward-continued and (b) downward-continued gravity data. Residuals of (c) upward-continued and (d) downward-continued gravity data. The residuals are defined as the difference between the true (not shown) and the continued gravity data. The insets in (c and d) show the histograms of residuals with their corresponding mean μ and standard deviation σ in mGal.

We used the vertical component of the gravitational attraction (Figure 10a) over the observation surface (Figure 10b) along flight lines at one sample per second. This data set was provided by Bell Geospace Inc. The flight lines are 250 m apart away from the dome and 125 m apart directly over the dome, with control lines spacing of 1 km (Figure 10c). To apply the fast equivalent-layer technique, we set the equivalent layer at a constant depth of 450 m. We use a similar approach as in the synthetic case and divide the survey area into three regions (I–III, Figure 10c) with different small areas to form the vector Δs that is used in equations 14 and 22. For regions I and III, we set an area of 13,403 m^2 and for region II, we set an area of 5710 m^2.

From the first approximation of the mass distribution ($\mathbf{m}^0$ in equation 28), the fast equivalent-layer technique estimates, at the 30th iteration, the final mass distribution (not shown) produced the predicted data shown in Figure 11a. The residuals (the difference between the observed and the predicted data) show a reasonable fit of the observed data (Figure 11b). Notice that the residuals have a mean close to zero and a standard deviation of 0.07 mGal (Figure 11c). These small residuals, for most of the study area, indicate that the estimated mass distribution can be used in the data processing.

Figure 11c and 11d shows the upward- and downward-continued gravity data, respectively (Figure 10a). Either the upward or the downward continuations were accomplished from the uneven observation surface (Figure 10b) to an uneven surface (not shown). The upward (downward) continuation was performed by subtracting (adding) from each z-coordinate of each observation point (Figure 10b) a constant value of 500 m (100 m). The continued results are reasonable because the upward-continued gravity data are more dominated by long wavelengths, whereas the downward-continued gravity data contain much short-wavelength variations. This real test totaled 11,494 observations. We stress that the number of flops required by the classic equivalent-layer technique (equations 33 and 34) is 2.02×10^{12}, whereas the fast iterative equivalent-layer technique requires 7.93×10^{9} flops (equation 35).

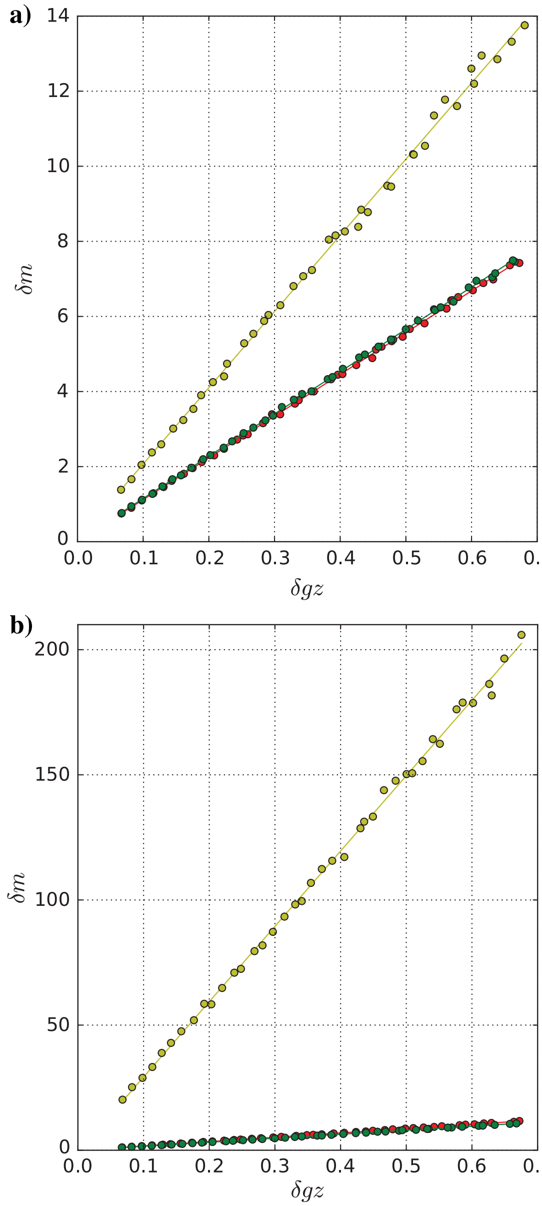

Figure 9. Stability tests with a grid of (a) 55×55 and (b) 85×85 observations. The horizontal and vertical axes represent the data and the parameter variations given in equations 36 and 37, respectively. The red, green, and yellow dots represent the 40 results obtained with the fast iterative equivalent-layer technique, the classic equivalent-layer technique with the zeroth-order Tikhonov regularization and the least-squares method, respectively. The red, green, and yellow lines represent the fitted straight lines whose estimated slopes are the condition numbers (κ in equation 38) obtained by applying a linear regression to the 40 results obtained with the fast iterative equivalent-layer technique (red dots), the classic equivalent-layer technique with the zeroth-order Tikhonov regularization (green dots), and least-squares method, respectively (yellow dots). The condition numbers of our method and the classic equivalent-layer technique with the zeroth-order Tikhonov regularization are very close to each other, demonstrating that our method yields stable solutions.

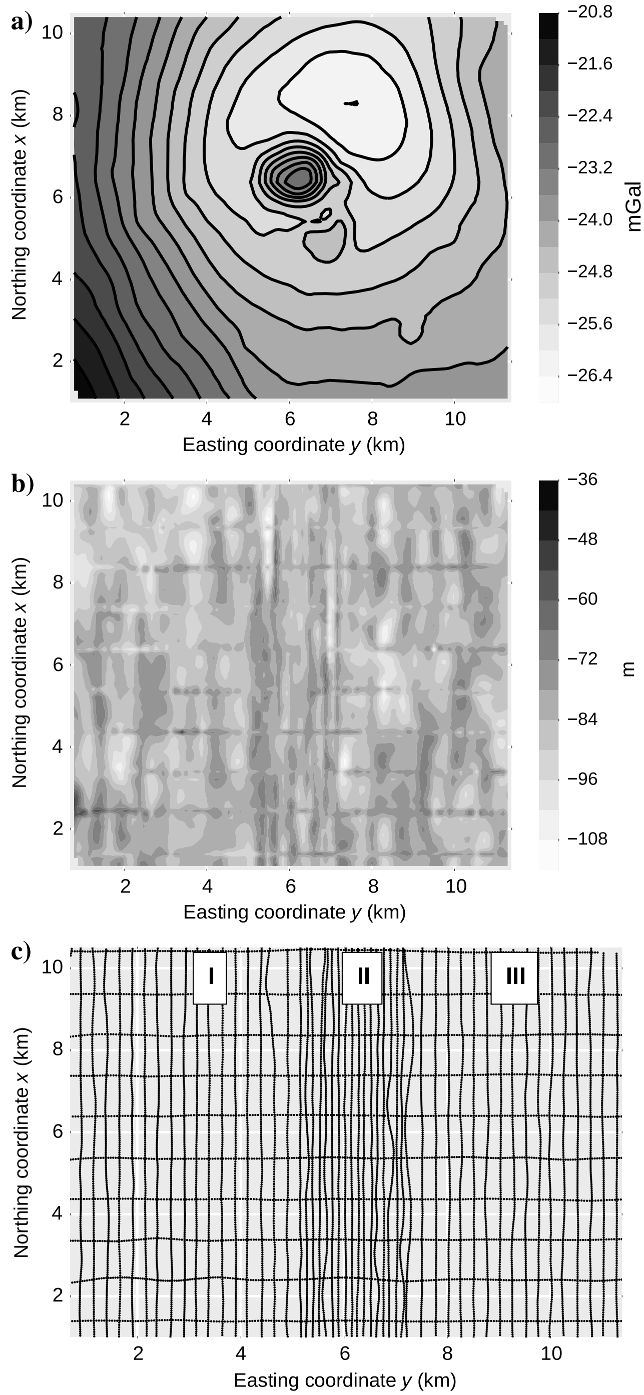

Figure 10. Vinton salt dome, Louisiana, USA. (a) Observed gravity data. (b) Observation surface. (c) Available flight lines.

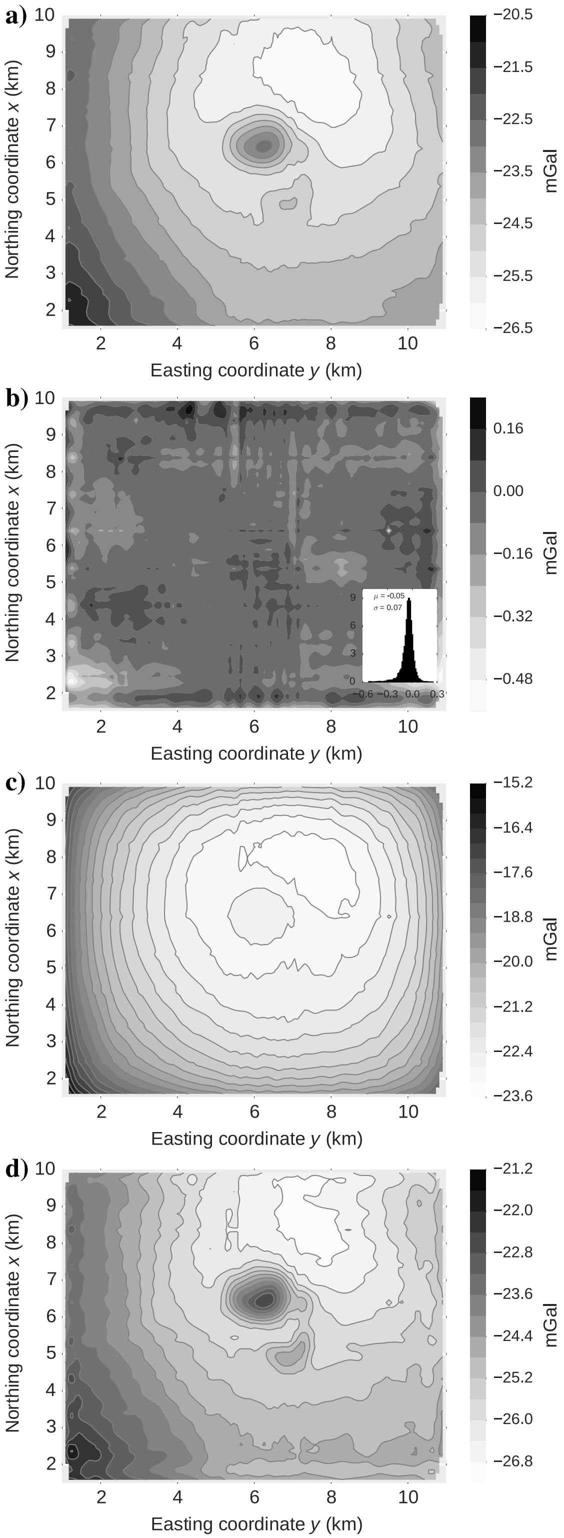

Figure 11. Vinton salt dome, Louisiana, USA. (a) Fitted gravity anomaly produced by the estimated mass distribution (not shown) with the fast equivalent-layer method. (b) Gravity residuals, defined as the difference between the observed gravity data in Figure 10a and the predicted data in panel (a). (b) Downward-continued and (c) upward-continued gravity data. The inset in panel (b) shows the histogram of gravity residuals shown in panel (b), with its mean μ and standard deviation σ in mGal.

CONCLUSIONS

We have developed a new fast iterative equivalent-layer technique for processing gravity data grounded on excess mass constraint. Our algorithm has low processing time and computer memory usage because there are neither matrix multiplications nor linear systems to be solved. We set up an equivalent layer with an ensemble of point masses, one directly beneath each observation point. Iteratively, our approach estimates the mass distribution that fits the gravity data within the measurement errors. Start with an initial approximation to a mass distribution proportional to the gravity observation; then, iteratively, we estimate a mass distribution correction that is proportional to the residual gravity anomaly. This mass distribution correction is the excess mass constraint. At each iteration, the ith mass correction, located beneath the ith gravity station, must partially explain the ith gravity residual. The positive correlation between the gravity data and the mass distribution over the equivalent layer guarantees the efficiency of the proposed iterative method. In this way, the larger the residual gravity anomaly, the larger the mass correction, hence, the better will be the fitted gravity data in the next iteration. We have accomplished a numerical analysis of the solution stability of the fast iterative equivalent-layer technique. This analysis reveals that this technique estimates stable mass distributions such as the classic equivalent-layer technique with the zeroth-order Tikhonov regularization.

Because our method sets one point mass per observation point, the number of gravity observations is crucial for its efficiency. It can fail for processing a small number of sparsely spaced gravity observations. Conversely, our method is fast and makes feasible the use of the equivalent-layer technique for processing large gravity data sets measured on uneven surfaces in which the Fourier-based methods are no longer valid. Tests on synthetic data confirmed the potential of our method in interpolating, calculating horizontal components, and upward (or downward) continuing the gravity data. Tests on field data from the Vinton salt dome, Louisiana, USA, confirm the potential of our approach in processing a large gravity data set over an undulating surface.

The fast iterative equivalent-layer technique is grounded on the excess mass constraint which in turn establishes that the total anomalous mass is proportional to the surface integration of the gravity data measured on a plane. Hence, this technique requires, theoretically, that the gravity data be measured on a horizontal plane. However, our results show that the technique works very well in the case of an uneven observation surface. In this way, future research is required to study the feasibility of applying this technique to data measured on a rugged observation surface.

ACKNOWLEDGMENTS

The authors thank the associate editor, F. Guspí, A. Salem, and an anonymous reviewer for their constructive comments. We are deeply indebted to the open-source Python toolkit for geophysical modeling and inversion (Uieda et al., 2013) called Fatiando a Terra (Portuguese for "slicing the earth"). We also acknowledge the open-source libraries (Jones et al., 2001) for array-based computations, matplotlib (Hunter, 2007), and seaborn (Waskom et al., 2015) for plots. Without the developers and maintainers of the mentioned open-source software, this work would not have been possible. The authors thank Bell Geospace Inc. for permission to use the real data from the Vinton salt dome. F.C L. Siqueira was supported by a scholarship from Coordenação de Aperfeiçoamento de Pessoal de Nvel Superior (CAPES). V.C.F. Barbosa was supported by fellowships from the Brazilian research agencies CNPQ (grant no. 307135/2014-4) and FAPERJ (grant no. E-26/203.091/2016 and E-26/203.594/2015).

REFERENCES

Aster, R. C., B. Borchers, and C. H. Thurber, 2005, Parameter estimation and inverse problems (international geophysics): Academic Press.

Barnes, G., and J. Lumley, 2011, Processing gravity gradient data: Geophysics, **76**, no. 2, I33–I47, doi: 10.1190/1.3548548.

Bhattacharyya, B. K., 1967, Some general properties of potential fields in space and frequency domain: A review: Geoexploration, **5**, 127–143, doi: 10.1016/0016-7142(67)90021-X.

Boggs, D. B., and M. H. Dransfield, 2004, Analysis of errors in gravity derived from the falcon airborne gravity gradiometer: ASEG-PESA Airborne Gravity 2004 Workshop, Geoscience Australia Record, 135–141.

Coker, M., J. Bhattacharya, and K. Marfurt, 2007, Fracture patterns within mudstones on the flanks of a salt dome: Syneresis or slumping?: Gulf Coast Association of Geological Societies, **57**, 125–137.

Cordell, L., 1992, A scattered equivalent-source method for interpolation and gridding of potential field data in three dimensions: Geophysics, **57**, 629–636, doi: 10.1190/1.1443275.

Dampney, C. N. G., 1969, The equivalent source technique: Geophysics, **34**, 39–53, doi: 10.1190/1.1439996.

Davis, K., and Y. Li, 2011, Fast solution of geophysical inversion using adaptive mesh, space-filling curves and wavelet compression: Geophysical Journal International, **185**, 157–166, doi: 10.1111/j.1365-246X.2011.04929.x.

Emilia, D. A., 1973, Equivalent sources used as an analytic base for processing total magnetic field profiles: Geophysics, **38**, 339–348, doi: 10.1190/1.1440344.

Ennen, C., and S. Hall, 2011, Structural mapping of the Vinton salt dome, Louisiana, using gravity gradiometry data: 81st Annual International Meeting, SEG, Expanded Abstracts, 830–835.

Grant, F., and G. West, 1965, Interpretation theory in applied geophysics: McGraw-Hill.

Guspí, F., and I. Novara, 2009, Reduction to the pole and transformations of scattered magnetic data using Newtonian equivalent sources: Geophysics, **74**, no. 5, L67–L73, doi: 10.1190/1.3170690.

Hansen, R. O., and Y. Miyazaki, 1984, Continuation of potential fields between arbitrary surfaces: Geophysics, **49**, 787–795, doi: 10.1190/1.1441707.

Henderson, R. G., 1960, A comprehensive system of automatic computation in magnetic and gravity interpretation: Geophysics, **25**, 569–585, doi: 10.1190/1.1438736.

Henderson, R. G., 1970, On the validity of the use of the upward continuation integral for total magnetic intensity data: Geophysics, **35**, 916–919, doi: 10.1190/1.1440137.

Hunter, J. D., 2007, Matplotlib: A 2D graphics environment: Computing in Science & Engineering, **9**, 90–95, doi: 10.1109/MCSE.2007.55.

Jones, E., T. Oliphant, and P. Peterson, 2001, SciPy: Open source scientific tools for PYTHON: http://www.scipy.org/, accessed 22 August 2015.

Kellogg, O. D., 1929, Foundations of potential theory: Frederick Ungar Publishing Company.

Lane, R., 2004, Integrating ground and airborne data into regional gravity compilation: ASEG-PESA Airborne Gravity 2004 Workshop, Geoscience Australia Record, 81–97.

Leão, J. W. D., and J. B. C. Silva, 1989, Discrete linear transformations of potential field data: Geophysics, **54**, 497–507, doi: 10.1190/1.1442676.

Li, Y., and D. W. Oldenburg, 2010, Rapid construction of equivalent sources using wavelets: Geophysics, **75**, no. 3, L51–L59, doi: 10.1190/1.3378764.

Mendonça, C. A., and J. B. C. Silva, 1994, The equivalent data concept applied to the interpolation of potential field data: Geophysics, **59**, 722–732, doi: 10.1190/1.1443630.

Menke, W., 1989, Geophysical data analysis: Discrete inverse theory: Academic Press Inc.

Oliveira, V. C., Jr., and V. C. F. Barbosa, 2013, 3-D radial gravity gradient inversion: Geophysical Journal International, **195**, 883–902, doi: 10.1093/gji/ggt307.

Oliveira, V. C., Jr., V. C. F. Barbosa, and L. Uieda, 2013, Polynomial equivalent layer: Geophysics, **78**, no. 1, G1–G13, doi: 10.1190/geo2012-0196.1.

Silva, J. B. C., 1986, Reduction to the pole as an inverse problem and its application to lowlatitude anomalies: Geophysics, **51**, 369–382, doi: 10.1190/1.1442096.

Strang, G., 1988, Linear algebra and its applications: Harcourt Brace Jonanovich.

Tikhonov, A. N., and V. Y. Arsenin, 1977, Solutions of ill-posed problems: V. H. Winston & Sons.

Uieda, L., V. C. Oliveira, Jr., and V. C. F. Barbosa, 2013, Modeling the earth with fatiando a terra: Proceedings of the 12th Python in Science Conference, 91–98.

Waskom, M., O. Botvinnik, P. Hobson, J. Warmenhoven, J. B. Cole, Y. Halchenko, J. Vanderplas, S. Hoyer, S. Villalba, E. Quintero, A. Miles, T. Augspurger, T. Yarkoni, C. Evans, D. Wehner, L. Rocher, T. Megies, L. P. Coelho, E. Ziegler, T. Hoppe, S. Seabold, S. Pascual, P. Cloud, M. Koskinen, C. Hausler, kjemmett, D. Milajevs, A. Qalieh, D. Allan, and K. Meyer, 2015, Seaborn: v0.6.0: 10.5281/zenodo.19108, accessed 2 November 2015.

Xia, J., and D. R. Sprowl, 1991, Correction of topographic distortion in gravity data: Geophysics, **56**, 537–541, doi: 10.1190/1.1443070.

Xia, J., D. R. Sprowl, and D. Adkins-Heljeson, 1993, Correction of topographic distortions in potential-field data: A fast and accurate approach: Geophysics, **58**, 515–523, doi: 10.1190/1.1443434.